Ultrastructural Alterations of Osteocyte Morphology via Loaded Implants in Rabbit Tibiae

Muneteru Sasaki [1], Shinichiro Kuroshima [1, *], Yuri Aoki, Nao Inaba, Takashi Sawase

Department of Applied Prosthodontics, Graduate School of Biomedical Sciences, Nagasaki University, Nagasaki, Japan

[*] Corresponding Author at: Department of Applied Prosthodontics, Graduate School of Biomedical Sciences, Nagasaki University, 1-7-1, Sakamoto, Nagasaki, 852-8588, Japan.
Tel.: +81 95 819 7688; fax: +81 95 819 7689.
E-mail address: kuroshima@nagasaki-u.ac.jp (S. Kuroshima).

[1] These authors contributed equally to this work.

KEY WORDS: Mechanical stress, Dendrites, Osteocytes, Dental implants, Scanning electron microscopy

Word count (Introduction through Discussion); 3,397 words

ABSTRACT

Osteocytes are crucial cells that control bone responses to mechanical loading. However, the effects of mechanical loading on osteocytes around dental implants are unclear. The aim of this study was to investigate whether mechanical loading via bone-integrated implants influences osteocyte number and morphology in the surrounding bone. Fourteen anodized Ti-6Al-4V alloy dental implants were placed in seven Japanese white rabbits, and implants in each rabbit were subjected to mechanical loading (50 N, 3 Hz for 1800 cycles, 2 days/week) along the implant long axis. Eight weeks after the initiation of loading, histomorphometric analysis and microcomputed tomography were performed. Scanning electron microscopy (SEM) was also performed with an acid etching technique using longitudinal and cross-sectional specimens. More bone formation around loaded implants was noted. In the implant neck, osteocytes tended to be more spherical with increased dendrite processes around loaded implants, while spindle-shaped osteocytes without increased dendrite processes were observed around unloaded implants in both longitudinal and cross-sectional images. In the bottom area, morphological changes in osteocytes were observed around loaded implants; however, dendrite processes did not differ in longitudinal or cross-sectional images, regardless of mechanical loading. These findings indicate that increased osteocyte numbers and developed dendrite processes are associated with anabolic bone responses to mechanical loading. The combination of acid etching and SEM imaging is a useful technique to assess ultrastructural osteocyte morphology around dental implants.

1. Introduction

Osteocytes elongate their dendrite processes and develop lacunar-canalicular systems that play an important role in bone remodeling (Zhang et al., 2006). Bone remodeling, which is essential for the maintenance of skeletal homeostasis, continues throughout life in response to dynamic and/or static loading such as gravity, functional movements, and exercises. Dynamic and static loading on bone tissue are converted to various mechanical stimuli, such as fluid shear stress, hydrostatic pressure and direct cellular deformation (Klein-Nulend et al., 2012), and osteocytes receive these stimuli through their dendrite processes within lacunar-canalicular systems, resulting in activation of signaling pathways that control bone reactions by producing bone formation and/or resorption proteins. Therefore, osteocytes and dendrite processes are crucial components of bone anabolic responses to mechanical loading (Bellido, 2014; Weinbaum et al., 1994).

Implant therapy is a reliable treatment option for replacing missing teeth. Long-term stability of peri-implant bone around dental implants is clinically essential for therapeutic success after functional loading (Albrektsson et al., 1986). Bone-integrated implants are subjected to functional and/or parafunctional stresses following connection with fixed or removable prostheses. Clinical and experimental reports indicate that dynamic loading increases bone-implant contact (BIC) and bone formation around dental implants, thus suggesting that bone remodeling around dental implants occurs in response to dynamic loading (Donati et al., 2013; Mavrogenis et al., 2009; Prati et al., 2013). In most implant studies, resin-embedded specimens including implants have been used, as decalcified tissue does not hold implants within the bone. Conventionally, BIC and bone area around dental implants are used for the evaluation of osseointegration and bone formation, respectively. However, it has recently been reported that the application of acid etching techniques on resin-embedded bone specimens with scanning electron microscopy (SEM) allows 3D observation of the canalicular network in order to quantitatively assess osteocyte networks in human bone (Milovanovic et al., 2013). Moreover, some studies have reported that the use of serial focused ion beam (FIB)/SEM or synchrotron-radiation-based X-ray computed tomography (SRCT) are effective for the quantitative 3D assessment of osteocyte

morphologies and networks (Langer et al., 2012; Pacureanu et al., 2012; Schneider et al., 2011). Nonetheless, the influence of dynamic loading on osteocytes in bone around dental implants is unclear.

Here, we employed an acid etching technique on resin-embedded bone tissue including dental implants in combination with SEM in order to observe the osteocytes around dental implants. The aim of this study was to investigate whether mechanical loading via bone-integrated implants influences osteocytes in the surrounding bone. We provide morphological evidence that repetitive mechanical loading via bone-integrated implants influences osteocytes, inducing a more spherical shape and increased dendrite processes. This may contribute to bone anabolic reactions around dental implants in response to mechanical loading.

2. Material and methods

2.1 Animal experiments

Seven adult female Japanese white rabbits weighing around 4.0 kg were used for experiments (Biotek Co., Ltd., Saga, Japan). Fourteen anodized Ti-6Al-4V alloy dental implants were obtained (3.7 x 6.0 mm; Kyocera Co., Kyoto, Japan). Twenty-eight Ti-6Al-4V screws (Kyocera) were used to anchor a custom-made loading device (Higuchi Co., Nagasaki, Japan). Implants and 2 anchor screws on each side of the implants were placed in the proximal tibial metaphysis unicortically under general anesthesia (35 mg/kg ketamine and 5 mg/kg xylazine cocktail). Load conditions were in accordance with our previous study (Kuroshima et al., 2015). Briefly, all implants had post abutments after 12 weeks of bone wound healing. Randomly selected implants from each rabbit were subjected to mechanical repetitive loading using a loading device supported by two lateral anchor screws on each implant under general anesthesia (n = 7, loading group). The load magnitude was 50 N with a frequency of 3 Hz for 1800 cycles, 2 days/week for 8 weeks (Fig. 1a and b). Load direction was parallel to the long axis of the implants. The remaining animals were not subjected to loading (n = 7, control group). Animal care and experimental procedures were performed in accordance with the Guidelines for Animal Experimentation of Nagasaki University, with approval from the Ethics Committee for Animal Research.

2.2 Microcomputed tomography (microCT) analysis

Rabbits were sacrificed at 8 weeks after the onset of loading. Tibial bone blocks including the implants and anchor screws were dissected with a diamond saw (Exakt®; Heraeus Kulzer GmbH, Hanau, Germany), and were fixed in 10% formalin for 48 hours. MicroCT was performed at a 20-μm voxel resolution with an energy level of 90 kV (R_mCT2; Rigaku Co., Tokyo, Japan). Bone around dental implants in the proximal tibial metaphysis was segmented and reconstructed using the semimanual contouring method in accordance with previous reports (Kuroshima et al., 2012) using TRI/3D-Bon (Ratoc System Engineering, Tokyo, Japan). Before segmentation, determination of threshold levels for bone and implants was performed by evaluating the upper and lower threshold levels for bone and implants based on the gray-scale histogram. Threshold levels of bone and implants did not overlap and allowed clear distinctions to be made. Means were calculated and used for every sample (Vandeweghe et al., 2013). Regions of interest (ROIs) were cross-sectionally located between 50 μm and 550 μm away from the implant surface in order to avoid metal-induced artifacts (Bernhardt et al., 2012), and were longitudinally located between the implant neck and 3.5 mm below the implant platform. Extracortical bone above the implant platform was excluded from the ROIs (Fig. 1c).

Bone volume fraction [BVF (%) = bone volume in ROI/tissue volume in ROI] was semi-automatically measured following the guideline for assessment of bone microstructure using microCT (Bouxsein et al., 2010).

2.3 Histomorphometric analysis

Tibial bone blocks were embedded in methyl methacrylate resin (Methyl methacrylate polymer and monomer; Wako Pure Chemical Industries, Ltd., Osaka, Japan) after gradual dehydration in ethanol. Resin-embedded samples were cut longitudinally to include the implant and anchor screws using an Exakt®, and were ground to a final thickness of around 15 μm. Toluidine blue staining was performed to detect bone formation around dental implants between 0 μm and 250 μm, and 250 μm and 500 μm away

from the implant surface, and from the implant neck to the inferior border of newly formed bone extending downward from the original cortex (Fig. 1d). Photomicrographs of stained sections were obtained by light microscopy (BZ-9000; Keyence, Osaka, Japan) and were histomorphometrically analyzed using a BZ Analyzer (Keyence, Osaka, Japan). Measurements were performed on each side of the implant, and mean values were calculated.

2.4 SEM analyses

SEM analyses were performed for the evaluation of ultrastructural osteocyte morphology in combination with an acid etching technique (Kubek et al., 2010; Milovanovic et al., 2013). After histomorphometric analyses, toluidine blue-stained specimens were also used for SEM analyses (longitudinal SEM images) (Fig. 2a). Remaining blocks without toluidine blue staining were cross-sectionally cut with Exakt® at approximately 50 µm below the implant platform, and the bottom area around the inferior border of newly formed bone area extending downward from the original cortex (cross-sectional SEM images) (Fig. 2a). Specimens were polished by sequential wet sanding using 500-, 800- and 1500-grit sandpapers (Sankyo-Rikagaku Co., Ltd., Saitama, Japan). The surface of polished samples was acid-etched in 9% phosphoric acid (Wako Pure Chemical Industries, Ltd.) for 20 seconds, treated with 5 % sodium hypochlorite for 5 minutes, rinsed with deionized distilled water, and completely dried using a desiccator (Sanyo Electric Co., Ltd., Tokyo, Japan) at 37°C for 24 hours. Specimens were mounted on aluminum discs (Nisshin EM Co., Ltd., Tokyo, Japan) using double-sided tape. Colloidal silver paste (Nisshin EM Co., Ltd.) was used for conduction. Sputter coating with gold (Ion Coater IB-3; Eiko Engineering Co., Ltd., Mito, Japan) was also performed for each experimental sample. SEM analysis was performed with an energy level of 15000 V and 70 mA (TM-1000; Hitachi Corp., Tokyo, Japan). Images were obtained for detection of osteocyte numbers, osteocyte ellipticity, and the number of osteocyte dendrite processes. Longitudinally, measurements were conducted at the neck and bottom area (Fig. 2a). Cross-sectionally, measurements were also conducted in three AOIs at the neck and bottom area (Fig. 2a). All osteocytes and dendrite processes in AOIs were counted manually, and data

analyses were semi-automatically performed using NIH image J 1.47. Each parameter was determined as follows: (1) osteocyte density (cells/mm^2) = number of osteocytes between 0 μm and 500 μm away from the implant surface at the neck, and between 0 μm and 250 μm away from the implant surface in the bottom area (AOIs; 500 μm x 500 μm and 250 μm x 250 μm, respectively) (Fig. 2a), (2) osteocyte ellipticity = aspect ratio of osteocytes at the neck and the bottom area (AOI; 500 μm x 500 μm and 250 μm x 250 μm, respectively). Ratio was calculated using the longest and the shortest lengths of each osteocyte (Fig. 2b), and (3) number of osteocyte dendrite processes (#/cell) = process numbers arising directly from cell membrane of osteocytes at the neck and bottom area (AOIs 500 μm x 500 μm, and 250 μm x 250 μm, respectively) (Fig. 2c). Ambiguous processes not arising from the cell membrane were not included in process numbers in this study. Measurements were performed on each side of the implant, and mean values were calculated.

2.5 Statistics

All analyses were performed in a blinded manner. Data were analyzed by the Shapiro-Wilk test for normality and paired t-test was conducted. Sample size was determined by power calculations to obtain 80% statistical power by referring to a published study in which similar experiments were performed (Pazzaglia et al., 2014). In the present study, “load effect” was defined as the adjusted ratio under loaded conditions for each value under non-loaded conditions. All statistical analyses were conducted with SYSTAT 13 (Systat Software, Chicago, IL). An α-level of 0.05 was considered to indicate statistical significance. Results are presented as means ± SEM.

3. Results

3.1 Effects of mechanical loading on bone formation around bone-integrated implants

All implants were histologically integrated without inflammation. Bone formation around dental implants was observed in toluidine blue-stained sections (Fig. 3a). More bone area in the loading group between 0 μm and 250 μm, and 250 μm and 500 μm away from the implant surface was noted when

compared with the control group. (Fig. 3b, Table 1). Bone mass around dental implants in the loading group was significantly higher on microCT (Fig. 3c and d, Table 1).

3.2 Effects of mechanical loading on osteocytes at the implant neck in longitudinal specimens.

In longitudinal images, the average number of osteocytes in the control and loading groups was 119.67 ± 14.87 and 192.33 ± 25.83, respectively (AOI: 500 μm x 500 μm). Mechanical loading significantly increased osteocyte density (Fig. 4a and b, Table 1). More spherical-shaped osteocytes were noted under loaded conditions. However, more spindle-shaped osteocytes were observed under non-loaded conditions (Fig. 4c and d, Table 1). Interestingly, the number of dendrite processes arising directly from the osteocyte cell membrane in the loading group was significantly higher when compared with control group (Fig. 4c and e, Table 1).

3.3 Effects of mechanical loading on osteocytes at the implant neck in cross-sectional specimens

In cross-sectional images, the average number of osteocytes in the control and loading groups was 133.33 ± 6.70 and 194.17 ± 20.31, respectively (AOIs: 500 μm x 500 μm). Mechanical loading significantly increased the density of spherical-shaped osteocytes with more dendrite processes (Fig. 5a-e, Table 1) when compared with the control group.

3.4 Influence of mechanical loading on osteocytes in the bottom area in longitudinal specimens.

In longitudinal images, the average number of osteocytes in the control and loading groups was 31.33 ± 3.33 and 43.00 ± 7.80, respectively (AOIs: 250 μm x 250 μm). Osteocyte numbers in the loading group were significantly higher than in the control group (Fig. 6a and b, Table 1). Mechanical loading significantly increased spherical-shaped osteocytes in the bone around dental implants (Fig. 6c and d), while the number of osteocyte dendrite processes was similar among the groups, regardless of mechanical loading (Fig. 6c and e).

3.5 Influence of mechanical loading on osteocytes in the bottom area of cross-sectional specimens

In cross-sectional images, the average number of osteocytes in the control and loading groups was 38.60 ± 2.20 and 66.17 ± 7.12, respectively (AOIs: 250 μm x 250 μm). Osteocyte numbers in the loading group were significantly higher than in the control group (Fig. 7a and b, Table 1). Mechanical loading significantly increased spherical-shaped osteocytes in the bone around dental implants (Fig. 7c and d, Table 1), while the number of osteocyte dendrite processes was similar among the groups, regardless of mechanical loading (Fig. 7c and e, Table 1).

3.6 Mechanical loading had different effects on osteocyte morphology between implant neck area and bottom area.

Longitudinally and cross-sectionally, the load effect on osteocyte ellipticity in the implant neck was stronger than in the bottom area (Fig. 8a and c). Moreover, the load effect on the number of osteocyte dendrite processes in the implant neck was larger than in the bottom area (Fig. 8b and d).

4. Discussion

We demonstrated that mechanical loading via bone-integrated implants influences the number of osteocyte dendrite processes and morphological changes. Moreover, we confirmed that osteocyte numbers in bone around dental implants were markedly increased by mechanical loading. Only two clinical studies have discussed the relationship between osteocytes and loaded dental implants, showing that dynamic loading, such as functional and parafunctional loading, increased osteocyte numbers under clinical conditions (Barros et al., 2009; Piattelli et al., 2014). They evaluated osteocyte density by counting osteocytes in the bone around dental implants using 30-μm resin-embedded sections stained with toluidine blue. However, accurately counting the number of osteocytes in such thick sections by light microscopy is challenging. In this study, osteocytes on the surface region of resin-embedded sections were investigated, thus suggesting that the measurements might be biased due to the 2D nature of the images. To overcome this problem, four areas around the implant neck were longitudinally and cross-

sectionally used to evaluate osteocyte morphology. One report has demonstrated that an acid etching technique in resin-embedded sections clearly visualizes the ultrastructural morphology of osteocytes (Milovanovic et al., 2013). Recently, SRCT has also been used to evaluate osteocytes. While the resolution of current SEM systems can be approximately 1 nm, most SRCT requires very small sections to achieve a resolution of 700 nm (Schneider et al., 2011). Hence, SEM analysis, but not SRCT, was used in the present study. Indeed, SEM images obtained using acid etching methods confirmed that osteocyte networks through their dendrite processes can be clearly observed. This indicates that a combination of the acid etching technique and SEM analysis is useful for investigating ultrastructural osteocyte morphology. This finding is also consistent with a previous study investigating osteocytes around dental implants without mechanical loading, although they did not use the 9% phosphoric acid etching method (Du et al., 2014).

Jaw bone was not used in this study. A previous report has demonstrated that the bone volume between tibiae and maxillae in female New Zealand white rabbits is almost the same (Slotte et al., 2003). Moreover, the application of a custom-made loading device to intraoral placement sites was technically challenging. In addition, the natural chewing frequency of New Zealand white rabbits is about 3.5 Hz (Peptan et al., 2008, Weijs and de Jongh, 1977), while another report found the frequency to be between 3.3 Hz and 4.0 Hz (Morimoto et al., 1985). Hence, rabbit tibiae were used, with a loading frequency of 3.0 Hz in the present study.

Immediate or early loading accelerates bone formation around dental implants (De Smet et al., 2006; Vandamme et al., 2007) due to synergistic effects of mechanical loading and wound healing after implant placement on bone. On the other hand, in rabbit tibiae, 8 to 12 weeks are necessary to re-establish normal bone architecture after surgical trauma (Breine et al., 1964; Danckwardt-Lilliestrom, 1969). Thus, the application of mechanical loading should be conducted after complete bone wound healing in order to clarify the net effects of mechanical loading on osteocyte morphology. In the present study, implants were subjected to mechanical loading at 12 weeks after implant placement, showing that accelerated bone formation and increased osteocytes with morphological changes around dental

implants were induced by mechanical loading via bone-integrated implants, but not bone wound healing. It is thought that load amplitude, frequency, rate, and duration are crucial factors in controlling bone reactions around dental implants. Load conditions in the present study were in accordance with those in a previous report (Kuroshima et al., 2015). Indeed, we confirmed that the load conditions increased bone formation around implants. However, a single load condition and time point was used. Moreover, the evaluation of load condition-dependent and time-dependent osteocyte changes under mechanical loading could not be performed. Thus, load condition is a limitation in this study.

Osteocytes, which exhibit cytoplasmic dendrite processes that form a network connecting neighboring osteocytes, are crucial mechanosensing cells that regulate bone anabolic/catabolic reactions to mechanical loading. They receive fluid shear stress, hydrostatic pressure, and direct cellular deformation, inducing bone reactions via activation of load-induced molecular signals (Klein-Nulend et al., 2012). In this study, neck area and bottom area were used for SEM analysis, as stress distribution occurs at both areas (Kitamura et al., 2004). However, dendrite processes directly from the cell membrane of osteocytes could not be completely detectable by SEM with the acid etching technique. Indeed, the number of dendrite processes in the present study was underestimated when compared with a previous study (Beno et al., 2006). On the other hand, osteocyte density under non-loaded conditions was overestimated when compared with previous reports (Mullender et al., 1996; Hedgecock et al., 2007). Implant placement may affect osteocyte density around dental implants. More spherical-shaped osteocytes with increased dendrite processes arising directly from the cell membrane were noted after mechanical loading, whereas more spindle-shaped osteocytes with no increase in dendrite processes were observed under non-loaded conditions. On the other hand, in the bottom area, mechanical loading increased the number of spherical-shaped osteocytes, but the number of osteocyte dendrite processes did not change, regardless of mechanical loading. These findings indicate that bone responses to mechanical stimuli via dental implants are site-specific. Indeed, calculated load effects on osteocyte morphology and the number of dendrite processes in the implant neck were longitudinally and cross-sectionally stronger when compared to those in the bottom area. These effects on osteocytes may be

related to the notion that the stress concentration at the neck area is greater than at the bottom area (Hudieb et al., 2011; Kitamura et al., 2004). In the present study, analyzed parameters in longitudinal images were almost the same as in cross-sectional images. Thus, it is thought that sample sectioning did not affect cell orientation. No unidirectional alignment of osteocytes was observed, regardless of mechanical loading in this study. Recent studies have reported that mouse fibular osteocytes showed elongated morphology with higher unidirectional alignment because the principle mechanical loading direction was parallel to the preferential alignment of osteocytes, while mouse calvarial osteocytes showed spherical-shaped morphology with random alignment in bone (Vatsa et al., 2008). In that study, mechanical loading was not applied, while mechanical loading was provided via dental implants in the present study. Thus, the influence of mechanical loading on osteocyte morphology and network development may be distinct among implant-mediated and -nonmediated bone microenvironments.

It has been demonstrated that mechanical loading opens osteocyte connexin (Cx) 43 hemichannels (Cherian et al., 2005). Cx 43 regulates load-mediated bone anabolism by controlling osteogenesis molecules and/or osteoclastogenesis molecules (Li et al., 2013). It has also been demonstrated that osteocyte dendrite processes play a crucial role in sensing mechanical loading, leading to the opening of osteocyte body's connexin 43 hemichannels (Burra et al., 2010). In addition, load-induced signaling molecules are transported to neighboring osteocytes through osteocyte dendrite processes (Bellido, 2014). Hence, both osteocyte bodies and their dendrite processes are key regulators of mechanical stimuli-induced bone reactions. In the present study, molecular mechanisms of osteocyte-induced bone responses to mechanical stimuli are not known, but our morphological findings suggest that osteocyte networks developed by increasing number of osteocytes and/or their dendrite processes in response to mechanical loading may contribute to enhanced bone formation around dental implants.

In summary, within the limitations of this study, we ultrastructurally demonstrated that mechanical loading via bone-integrated implants increased the number of spherical-shaped osteocytes in bone around dental implants, and increased osteocyte dendrite processes in the implant neck. Accelerated

osteocyte responses to mechanical loading via bone-integrated implants may be associated with increased bone anabolism.

Conflict of interest statement

The authors have no conflicts of interest.

Acknowledgements

The authors would like to thank Dr. Munenori Yasutake for assistance with animal experiments. This work was supported by a Grant-in Aid for Science Research (B) from the Japan Society for the Promotion of Science (#22390368).

REFERENCES

Albrektsson, T., Zarb, G., Worthington, P., Eriksson, A. R., 1986. The long-term efficacy of currently used dental implants: A review and proposed criteria of success. Int. J. Oral Maxillofac. Implants 1, 11-25.

Barros, R. R., Degidi, M., Novaes, A. B., Piattelli, A., Shibli, J. A., Iezzi, G., 2009. Osteocyte density in the peri-implant bone of immediately loaded and submerged dental implants. J. Periodontol. 80, 499-504.

Bellido, T., 2014. Osteocyte-driven bone remodeling. Calcif. Tissue Int. 94, 25-34.

Beno, T., Yoon, Y. J., Cowin, S. C., Fritton, S. P., 2006. Estimation of bone permeability using accurate microstructural measuraments. 39, 2378-2387.

Bernhardt, R., Kuhlisch, E., Schulz, M. C., Eckelt, U., Stadlinger, B., 2012. Comparison of bone-implant contact and bone-implant volume between 2d-histological sections and 3d-srµct slices. Eur. Cell. Mater. 23, 237-247; discussion 247-248.

Bouxsein, M. L., Boyd, S. K., Christiansen, B. A., Guldberg, R. E., Jepsen, K. J., Müller, R., 2010. Guidelines for assessment of bone microstructure in rodents using micro-computed tomography. J. Bone Miner. Res. 25, 1468-1486.

BREINE, U., JOHANSSON, B., ROYLANCE, P. J., ROECKERT, H., YOFFEY, J. M., 1964. Regeneration of bone marrow. A clinical and experimental study following removal of bone marrow by curettage. Acta Anat. (Basel) 59, 1-46.

Burra, S., Nicolella, D. P., Francis, W. L., Freitas, C. J., Mueschke, N. J., Poole, K., et al., 2010. Dendritic processes of osteocytes are mechanotransducers that induce the opening of hemichannels. Proc. Natl. Acad. Sci. USA 107, 13648-13653.

Cherian, P. P., Siller-Jackson, A. J., Gu, S., Wang, X., Bonewald, L. F., Sprague, E., et al., 2005. Mechanical strain opens connexin 43 hemichannels in osteocytes: A novel mechanism for the release of prostaglandin. Mol. Biol. Cell 16, 3100-3106.

Danckwardt-Lilliestrom, G., 1969. Reaming of the medullary cavity and its effect on diaphyseal bone. A fluorochromic, microangiographic and histologic study on the rabbit tibia and dog femur. Acta Orthop. Scand. Suppl. 128, 1-153.

De Smet, E., Jaecques, S. V., Wevers, M., Jansen, J. A., Jacobs, R., Sloten, J. V., et al., 2006. Effect of controlled early implant loading on bone healing and bone mass in guinea pigs, as assessed by micro-ct and histology. Eur. J. Oral Sci. 114, 232-242.

Donati, M., Botticelli, D., La Scala, V., Tomasi, C., Berglundh, T., 2013. Effect of immediate functional loading on osseointegration of implants used for single tooth replacement. A human histological study. Clin. Oral Implants Res. 24, 738-745.

Du, Z., Ivanovski, S., Hamlet, S. M., Feng, J. Q., Xiao, Y., 2014. The ultrastructural relationship between osteocytes and dental implants following osseointegration. Clin. Implant Dent. Relat. Res. doi: 10.1111/cid.12257. [Epub ahead of print]

Hedgecock, N. L., Hadi, T., Chen, A. A., Curtiss, S. B., Martin, R. B., Hazelwood, S. J., 2007. Quantitative regional associations between remodeling, modeling, and osteocyte apoptosis and denstiy in rabbit tibial midshafts. Bone. 40, 627-637.

Hudieb, M. I., Wakabayashi, N., Kasugai, S., 2011. Magnitude and direction of mechanical stress at the osseointegrated interface of the microthread implant. J. Periodontol. 82, 1061-1070.

Kitamura, E., Stegaroiu, R., Nomura, S., Miyakawa, O., 2004. Biomechanical aspects of marginal bone resorption around osseointegarated implants: considerations based on a three-dimensional finite element analysis. Clin. Oral Implants Res. 15, 401-412.

Klein-Nulend, J., Bacabac, R. G., Bakker, A. D., 2012. Mechanical loading and how it affects bone cells: The role of the osteocyte cytoskeleton in maintaining our skeleton. Eur. Cell. Mater. 24, 278-291.

Kubek, D. J., Gattone, V. H., Allen, M. R., 2010. Methodological assessment of acid-etching for visualizing the osteocyte lacunar-canalicular networks using scanning electron microscopy. Microsc. Res. Tech. 73, 182-186.

Kuroshima, S., Virginia-Arlene, A. Go., Yamashita, J., 2012. Increased numbers of tartrate-resistant acid phosphatase positive cells on long-term zoledronic acid therapy in mice. Endocrinology 153, 17-28.

Kuroshima, S., Yasutake, M., Tsuiki, K., Nakano, T., Sawase, T., 2015. Structural and qualitative bone remodeling around repetitive loaded implants in rabbits. Clin. Implant Dent. Relat. Res. [Epub ahead of print].

Langer, M., Pacureanu, A., Suhonen, H., Grimal, Q., Cloetens, P., Peyrin, F., 2012. X-ray phase nanotomography resolves the 3D human bone ultrastructure. PLoS One. 7, 235691.

Li, X., Liu, C., Li, P., Li, S., Zhao, Z., Chen, Y., et al., 2013. Connexin 43 is a potential regulator in fluid shear stress-induced signal transduction in osteocytes. J. Orthop. Res. 31, 1959-1965.

Mavrogenis, A. F., Dimitriou, R., Parvizi, J., Babis, G. C., 2009. Biology of implant osseointegration. J. Musculoskelet. Neuronal Interact. 9, 61-71.

Milovanovic, P., Zimmermann, E. A., Hahn, M., Djonic, D., Püschel, K., Djuric, M., et al., 2013. Osteocytic canalicular networks: Morphological implications for altered mechanosensitivity. ACS Nano 7, 7542-7551.

Morimoto, T., Inoue, T., Nakamura, T., Kawamura, Y.,1985. Characteristics of rhythmic jaw movements of the rabbit. Arch. Oral Biol. 30, 673-677.

Mullender, M. G., Huiskes, R., Versleyen, H., Buma, P., 1996. Osteocyte density and histomorphometric parameters in cancellous bone of the proximal femur in five mammalian species. J. Orthop. Res. 14, 972-979.

Pazzaglia, U. E., Congiu, T., Sibilia, V., Quacci, D., 2014. Osteoblast-osteocyte transformation. A SEM densitometric analysis of endosteal apposition in rabbit femur. J. Anat. 224, 132-141.

Peptan, A. I., Lopez, A., Kopher, R. A., Mao, J. J., 2008. Responses of intramembranous bone and sutures upon in vivo cyclic tensile and compressive loading. Bone. 42, 432-438.

Pacureanu, A., Langer, M., Boller, E., Tafforeau, P., Peyrin, F., 2012. Nanoscale imaging of the bone cell network with synchroton X-ray tomography: optimization of acuision setup. Med. Phys. 39, 2229-2238.

Piattelli, A., Artese, L., Penitente, E., Iaculli, F., Degidi, M., Mangano, C., et al., 2014. Osteocyte density in the peri-implant bone of implants retrieved after different time periods (4 weeks to 27 years). J. Biomed. Mater. Res. B Appl. Biomater. 102, 239-243.

Prati, A. J., Casati, M. Z., Ribeiro, F. V., Cirano, F. R., Pastore, G. P., Pimentel, S. P., et al., 2013. Release of bone markers in immediately loaded and nonloaded dental implants: A randomized clinical trial. J. Dent. Res. 92, 161S-167S.

Schneider, P., Meier, M., Wepf, R., Müller, R., 2011. Serial FIB/SEM imaging for quantitative 3D assesment of the osteocyte lacuno-canalicular network. Bone. 49, 304-311.

Slotte, C., Lundgren, D., Sennerby, L., Lundgren, A. K,. 2003. Surgical intervention in enchondral and membranous bone: intraindividual comparisons in the rabbit. Clin. Implant. Dent. Relat. Res. 5, 263-268.

Vandamme, K., Naert, I., Geris, L., Vander Sloten, J., Puers, R., Duyck, J. 2007. Influence of controlled immediate loading and implant design on peri-implant bone formation. J. Clin. Periodontol. 34, 172-181.

Vandeweghe, S., Coelho, P. G., Vanhove, C., Wennerberg, A., Jimbo, R. 2013. Utilizing micro-computed tomography to evaluate bone structure surrounding dental implants. A comparison with histomorphoetry. J. Biomed. Mater. Res. B Appl. Biomater. [Epub ahead of print]

Vatsa, A., Breuls, R. G., Semeins, C. M., Salmon, P. L., Smit, T. H., Klein-Nulend, J., 2008. Osteocyte morphology in fibula and calvaria --- is there a role for mechanosensing? Bone. 43, 452-458.

Weijs, W. A, de Jongh, H. J., Strain in mandibular alveolar bone during mastication in the rabbit. 1977. Arch. Oral Biol. 22, 667-675.

Weinbaum, S., Cowin, S. C., Zeng, Y., 1994. A model for the excitation of osteocytes by mechanical loading-induced bone fluid shear stresses. J. Biomech. 27, 339-360.

Zhang, K., Barragan-Adjemian, C., Ye, L., Kotha, S., Dallas, M., Lu, Y., et al., 2006. E11/gp38 selective expression in osteocytes: Regulation by mechanical strain and role in dendrite elongation. Mol. Cell Biol. 26, 4539-4552.

FIGURE LEGENDS

Table 1. Mean values and P values for each analyzed parameter.

Fig. 1. Experimental design and area/region of interest in each analysis. (a) Randomly selected implants from each rabbit underwent repetitive mechanical loading for 12 weeks after implant placement (n=7, loading group). The remaining implants were not subjected to loading (n=7, control group). (b) A custom-made loading device supported by two anchor screws provided mechanical loading along the implant axis (arrow). Distance between the implant surface and the screw surface was 2 mm. (c) Site of microCT imaging and ROI for the analysis of bone volume. ROI was cross-sectionally between 50 μm and 550 μm away from the implant surface, and longitudinally between the implant neck and 3.5 mm from the implant neck (dotted white and black line indicate top of the implant). (d) Toluidine blue staining. Each colored area between 0 μm and 250 μm (surrounded by blue line), and between 250 μm and 500 μm (surrounded by yellow line) away from the implant surface, and from the implant neck to the inferior border of newly formed bone extending downward from the original cortex, was used for detection of bone formation around dental implants (dotted line indicates top of the implant).

Fig. 2. SEM and segmented images. (a) AOIs for SEM analyses. Longitudinally, SEM observation was performed at approximately 50 μm below the implant platform, and the top of the “bottom area” around the inferior border of newly formed bone area extending downward from the original cortex [AOI: 500 μm x 500 μm (surrounded by yellow line) and 250 μm x 250 μm (surrounded by red line), respectively]. Cross-sectionally, SEM observation was also conducted at the implant neck and bottom area [AOIs: 500 μm x 500 μm (surrounded by yellow line) and 250 μm x 250 μm (surrounded by red line), respectively]. Osteocyte density was measured at the implant neck and bottom area. Longitudinally, measurement was performed for each area. Cross-sectionally, assessment was conducted by averaging the measurement values for three AOIs [AOI: 500 μm x 500 μm at neck area (surrounded by yellow line) and 250 μm x 250 μm at bottom area (surrounded by red line).] Bar = 500 μm. (b) Aspect ratio was calculated (yellow-green:

osteocyte morphology; red lines: longest and shortest osteocyte length) using longitudinal and cross-sectional SEM images (AOI: 500 μm x 500 μm at neck area, and 250 μm x 250 μm at bottom area). (c) Osteocyte dendrite numbers was also counted at the implant neck area and bottom area. Outlines of cell membranes for each osteocyte were drawn (yellow-green). Dendrites arising directly from cell membranes were also drawn (red line) and manually counted. Dendrites not arising directly from cell membranes were excluded from analysis. (AOI: 500 μm x 500 μm at neck area, and 250 μm x 250 μm at bottom area).

Fig. 3. Mechanical loading increased bone mass around dental implants. (a) Representative longitudinal images of toluidine blue-stained sections. Bar = 1 mm. (b) Bone formation area between 0 μm and 250 μm away from the implant surface in the loading group was significantly higher when compared with the control group. Bone formation area between 250 μm and 500 μm away from the implant surface was also significantly higher in the loading group. (c) Representative longitudinal images of microCT scans. Longitudinal ROI is indicated by dotted yellow line (500 μm x 3500 μm). Bar = 500 μm. (d) Bone volume fraction (BVF) in the loading group was significantly higher when compared with the control group.

Fig. 4. Ultrastructural changes in osteocytes at the implant neck in longitudinal SEM images. (a) Representative SEM images with lower magnification (white asterisk: bone marrow; black asterisk: dental implant; yellow-green: osteocytes; aqua: dental implant). Bar = 100 μm. (b) Osteocyte density in the loading group was significantly higher when compared with the control group. (c) Representative SEM images with higher magnification (dendrite processes were colored). Bar = 10 μm. (d) Osteocyte ellipticity was significantly smaller in the loading group than in the control group. (e) Number of dendrite processes of osteocytes was significantly larger in the loading group than in the control group.

Fig. 5. Ultrastructural changes in osteocytes at the neck in cross-sectional SEM images. (a) Representative cross-sectional SEM images with lower magnification (white asterisk: bone marrow; black

asterisk: dental implant; yellow-green: osteocytes; aqua: dental implant). Bar = 100 μm. (b) Osteocyte density in the loading group was significantly bigger than control. (c) Representative SEM images with higher magnification (dendrite processes were colored). Bar = 10 μm. (d) Osteocyte ellipticity in the loading group was significantly smaller. (e) More dendrite processes were noted in the loading group.

Fig. 6. Ultrastructural changes in osteocytes in the bottom area in longitudinal SEM images. (a) Representative longitudinal SEM images with lower magnification (white asterisk: bone marrow; black asterisk: dental implant; yellow-green: osteocytes; aqua: dental implant). Bar = 100 μm. (b) Osteocyte numbers in the loading group were significantly higher when compared with the control group. (c) Representative SEM images with higher magnification (dendrite processes were colored). Bar = 10 μm. (d) Osteocyte ellipticity was significantly smaller in the loading group than that in the control group. (e) Number of dendrite processes in the loading group was similar to that in the control group.

Fig. 7. Ultrastructural changes in osteocytes in the bottom area in cross-sectional SEM images. (a) Representative cross-sectional SEM images with lower magnification (white asterisk: bone marrow; black asterisk: dental implant; yellow-green: osteocytes; aqua: dental implant). Bar = 100 μm. (b) Osteocyte numbers in the loading group were significantly increased. (c) Representative SEM images with higher magnification (dendrite processes were colored). Bar = 10 μm. (d) Osteocyte ellipticity was significantly smaller in the loading group. (e) Number of dendrite processes in the loading group was similar to that in the control group.

Fig. 8. Load effects on each assessment parameter in the neck and bottom area. Longitudinally, (a) Load effects on osteocyte ellipticity were smaller in the bottom area than in the neck area, and (b) Load effects on the number of osteocyte dendrite processes were larger in the neck area than in the bottom area. Cross-sectionally, (c) Load effects on osteocyte ellipticity were smaller in the bottom area, and (d) Load effects on the number of osteocyte dendrite processes were larger in the neck area.

Table 1
Mean values and *P* value for each analyzed parameter

	Control (Mean± SEM)	Loading (Mean± SEM)	*P* value
Histological Images (Histology)			
Bone formation 0-250 μm (mm^2)	0.43±0.03	0.55±0.05	0.028
Bone formation 250-500 μm (mm^2)	0.35±0.03	0.51±0.03	0.003
Micro CT)			
BVF (%)	15.572±2.683	38.406±3.141	0.000
Implant neck area			
Longitudinal SEM images			
Osteocyte density (#/mm^2)	835.25±79.64	1191.24±85.24	0.019
Osteocyte ellipticity	2.80±0.27	1.63±0.07	0.006
Dendrite numbers (#/cell)	21.02±1.24	28.39±2.75	0.042
Cross-sectional SEM images			
Osteocyte density (#/mm^2)	699.34±36.82	969.28±36.39	0.000
Osteocyte ellipticity	2.50±0.22	1.81±0.03	0.026
Dendrite numbers (#/cell)	12.11±3.04	18.66±2.34	0.040
Bottom area			
Longitudinal images			
Osteocyte density (#/mm^2)	937.03±109.40	1604.54±101.33	0.003
Osteocyte ellipticity	2.26±0.24	1.55±0.07	0.016
Dendrite numbers (#/cell)	14.33±1.81	15.40±1.65	0.647
Cross-sectional images			
Osteocyte density (#/mm^2)	816.29±36.61	1124.11±126.25	0.031
Osteocyte ellipticity	2.64±0.19	1.92±0.21	0.036
Dendrite numbers (#/cell)	17.67±4.10	20.07±1.45	0.495

Fig. 1.

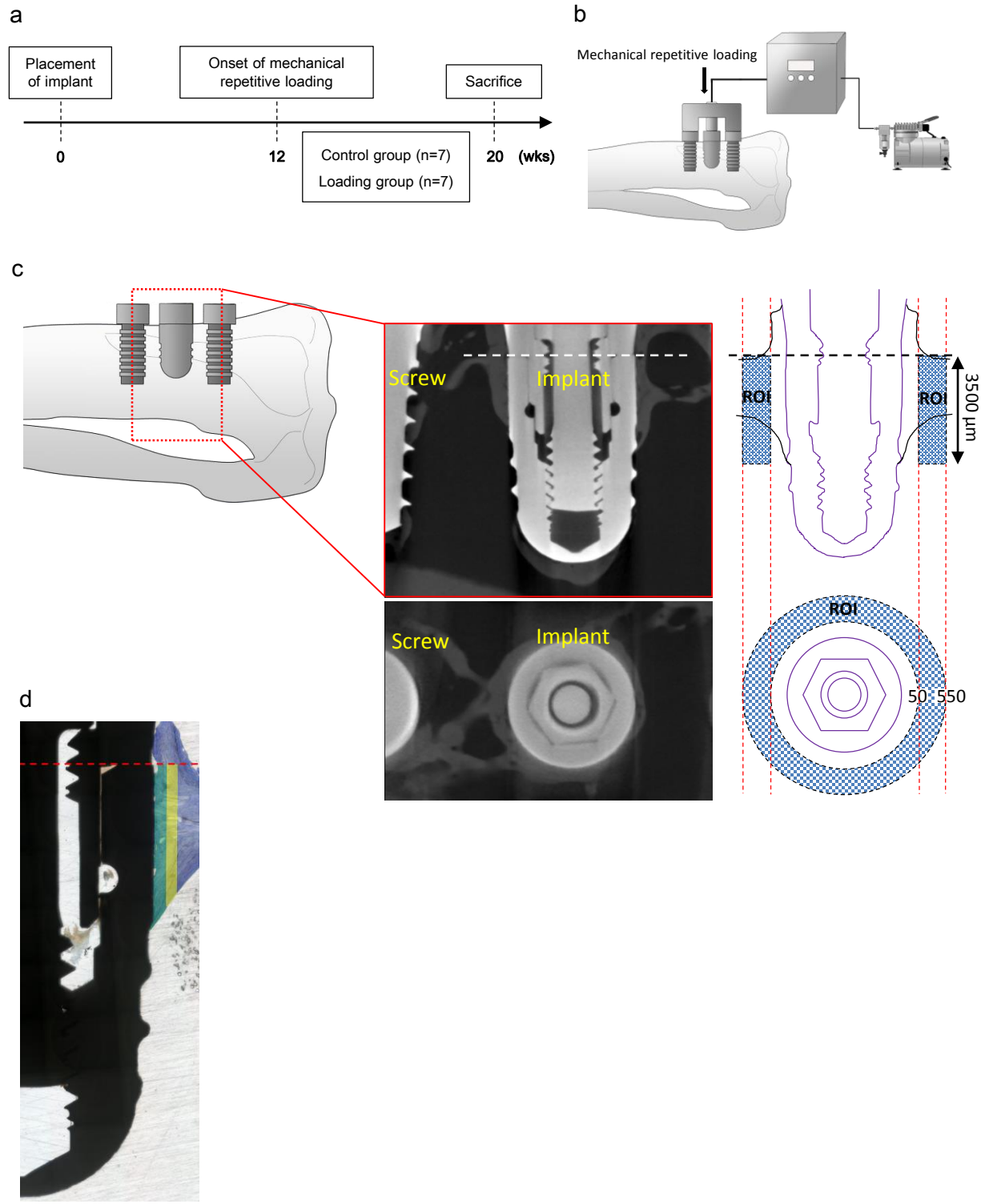
a
Placement of implant
Onset of mechanical repetitive loading
Sacrifice
0
12
20 (wks)
Control group (n=7)
Loading group (n=7)
b
Mechanical repetitive loading
c
Screw
Implant
Screw
Implant
ROI
ROI
3500 μm
ROI
50
550
d

Fig. 2.

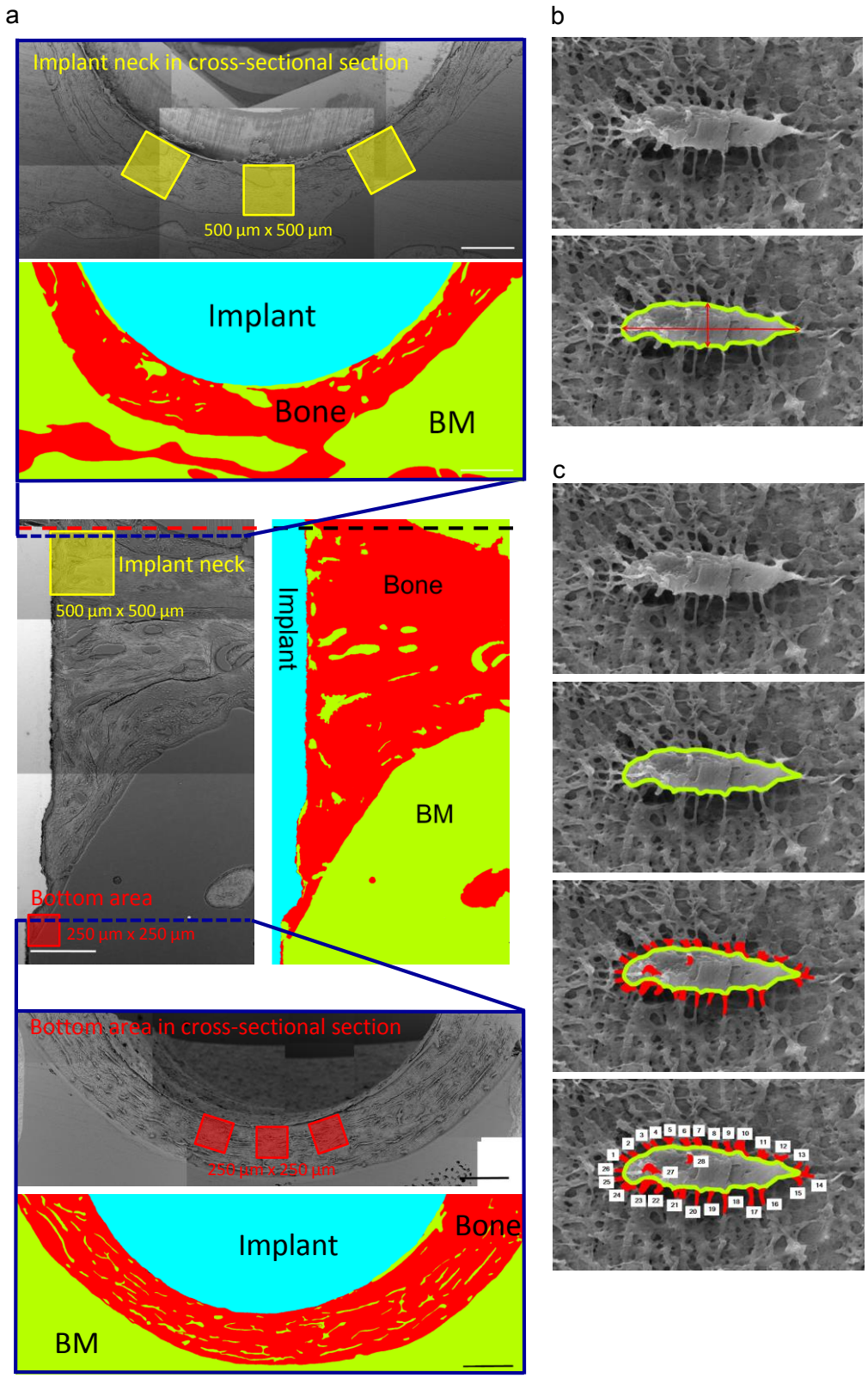
a
Implant neck in cross-sectional section
500 µm x 500 µm
Implant
Bone
BM
Implant neck
500 µm x 500 µm
Implant
Bone
BM
Bottom area
250 µm x 250 µm
Bottom area in cross-sectional section
250 µm x 250 µm
Implant
Bone
BM
b
c

Fig. 3.

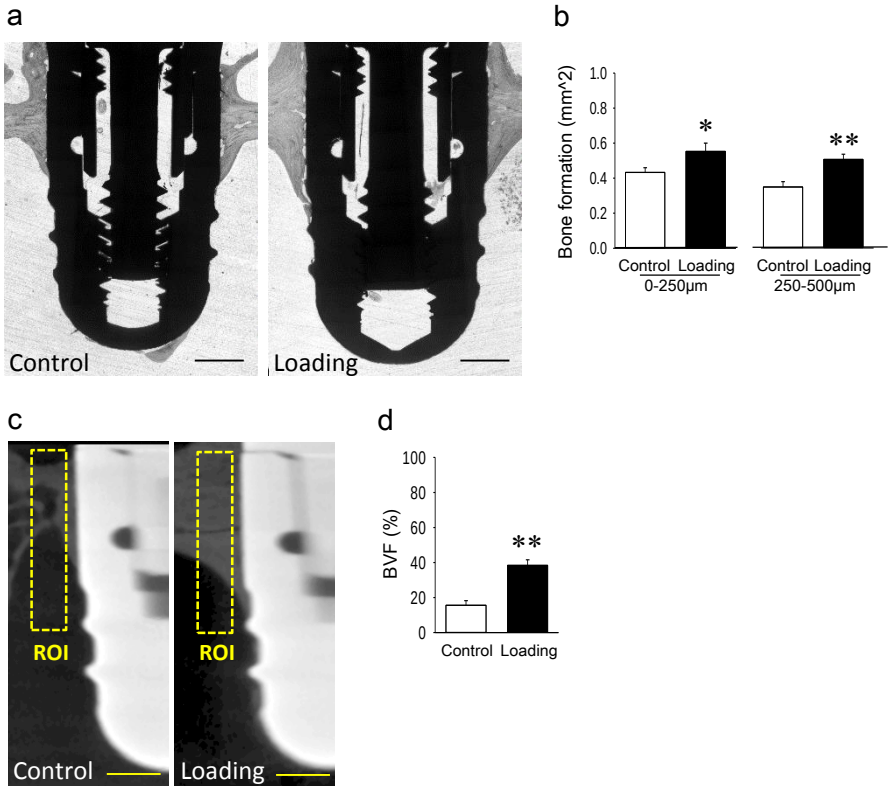
a
Control
Loading
b
Bone formation (mm^2)
1.0
0.8
0.6
0.4
0.2
0.0
*
**
Control Loading
0-250μm
Control Loading
250-500μm
c
ROI
ROI
Control
Loading
d
BVF (%)
100
80
60
40
20
0
**
Control Loading

Fig. 4.

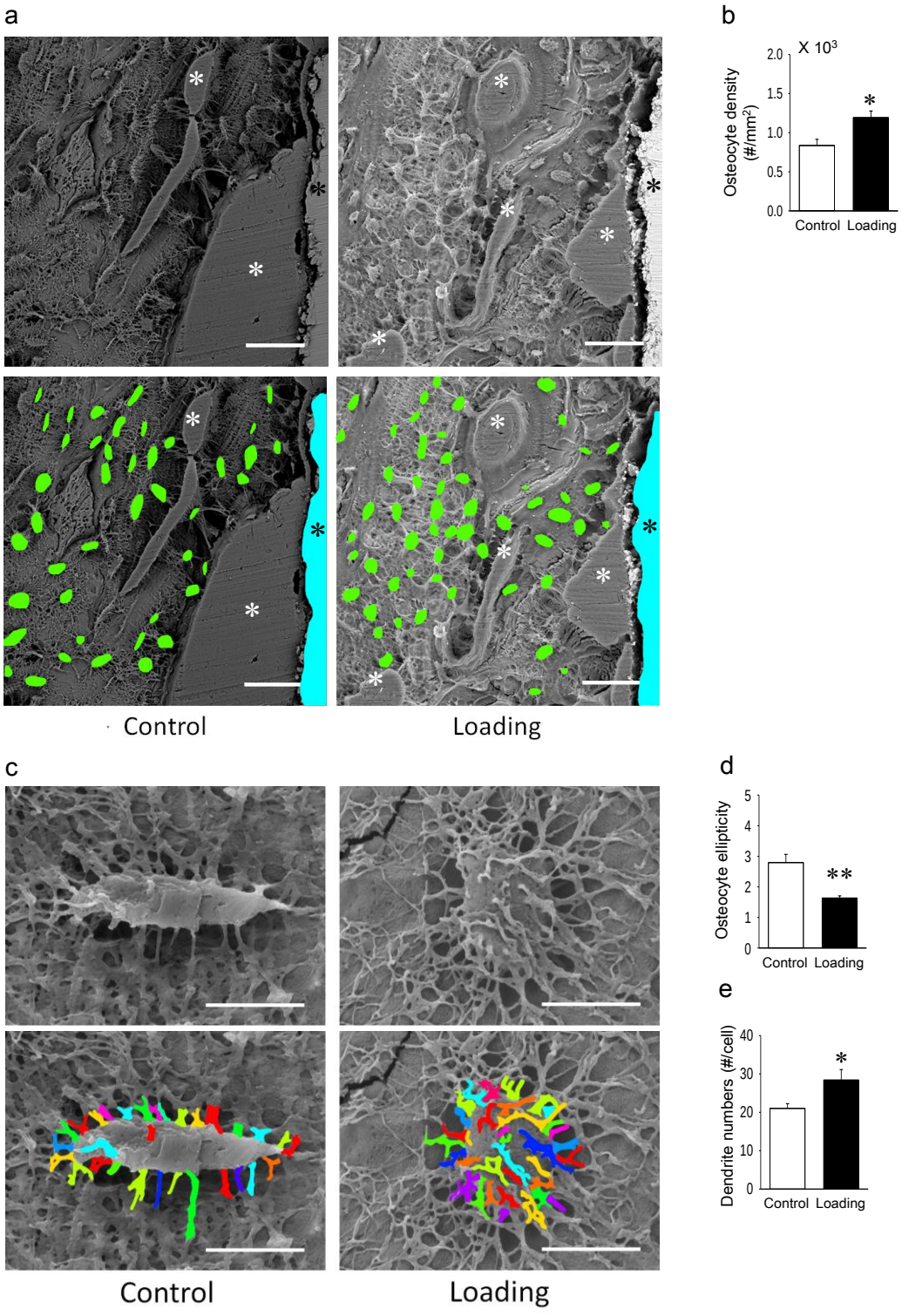
a
b
X 10³
Osteocyte density (#/mm²)
2.0
1.5
1.0
0.5
0.0
Control
Loading
Control
Loading
c
d
Osteocyte ellipticity
5
4
3
2
1
0
**
Control
Loading
e
Dendrite numbers (#/cell)
40
30
20
10
0
*
Control
Loading
Control
Loading

Fig. 5.

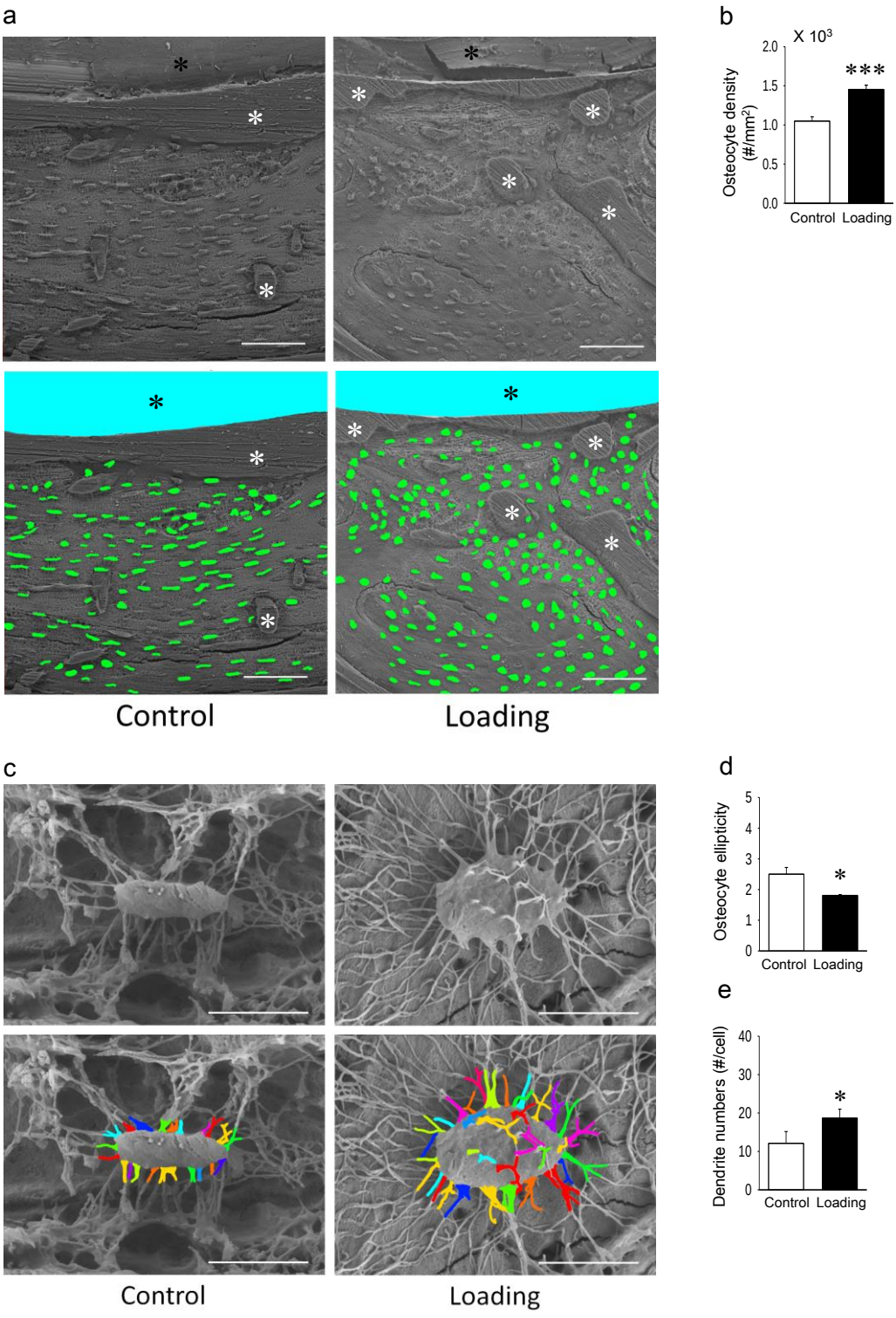
a
b
X 10³
Osteocyte density (#/mm²)
2.0
1.5
1.0
0.5
0.0
***
Control
Loading
Control
Loading
c
d
Osteocyte ellipticity
5
4
3
2
1
0
*
Control
Loading
e
Dendrite numbers (#/cell)
40
30
20
10
0
*
Control
Loading
Control
Loading

Fig. 6.

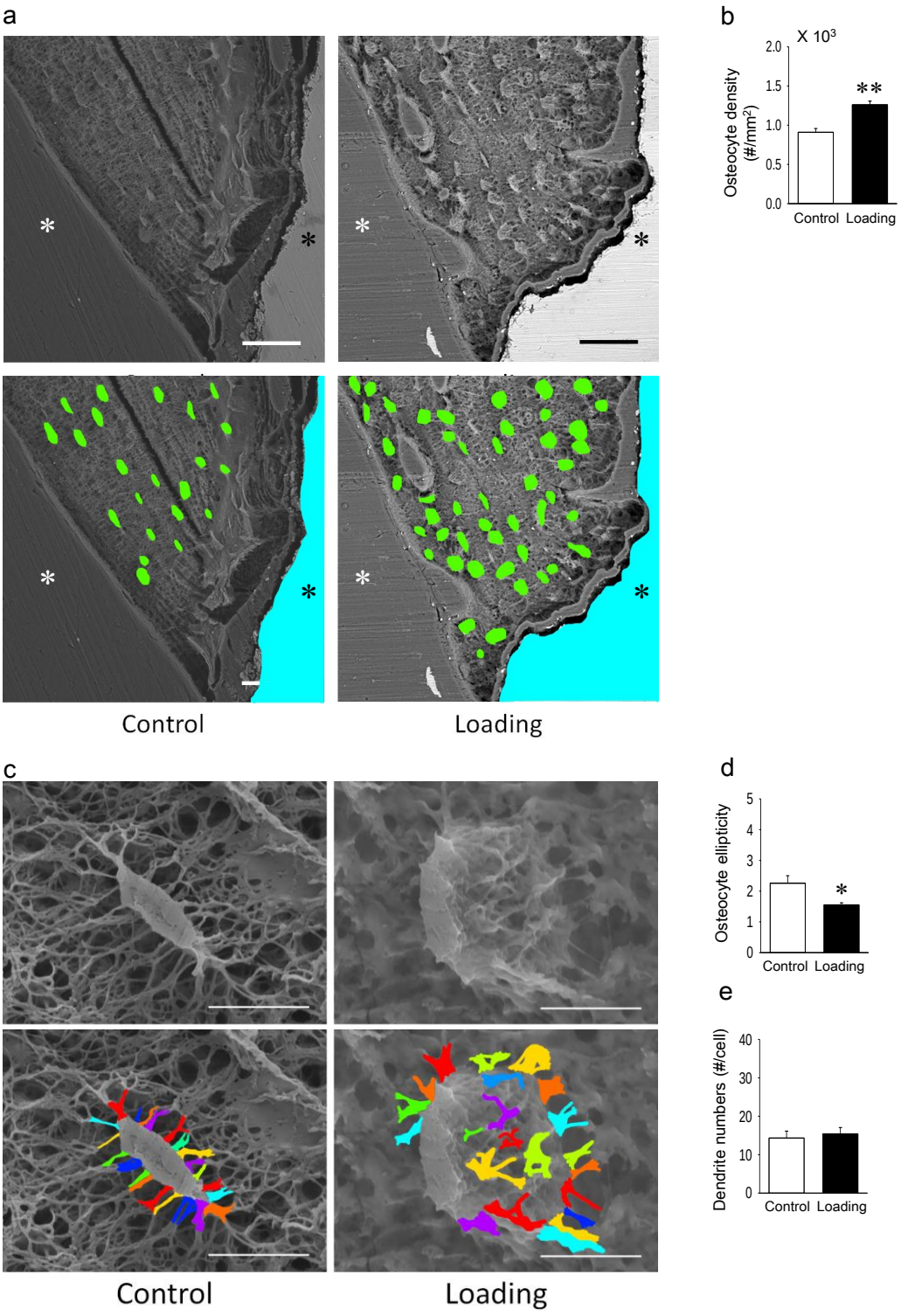
a
b
X 10³
Osteocyte density (#/mm²)
2.0
1.5
1.0
0.5
0.0
**
Control
Loading
Control
Loading
c
d
Osteocyte ellipticity
5
4
3
2
1
0
*
Control
Loading
e
Dendrite numbers (#/cell)
40
30
20
10
0
Control
Loading
Control
Loading

Fig. 7.

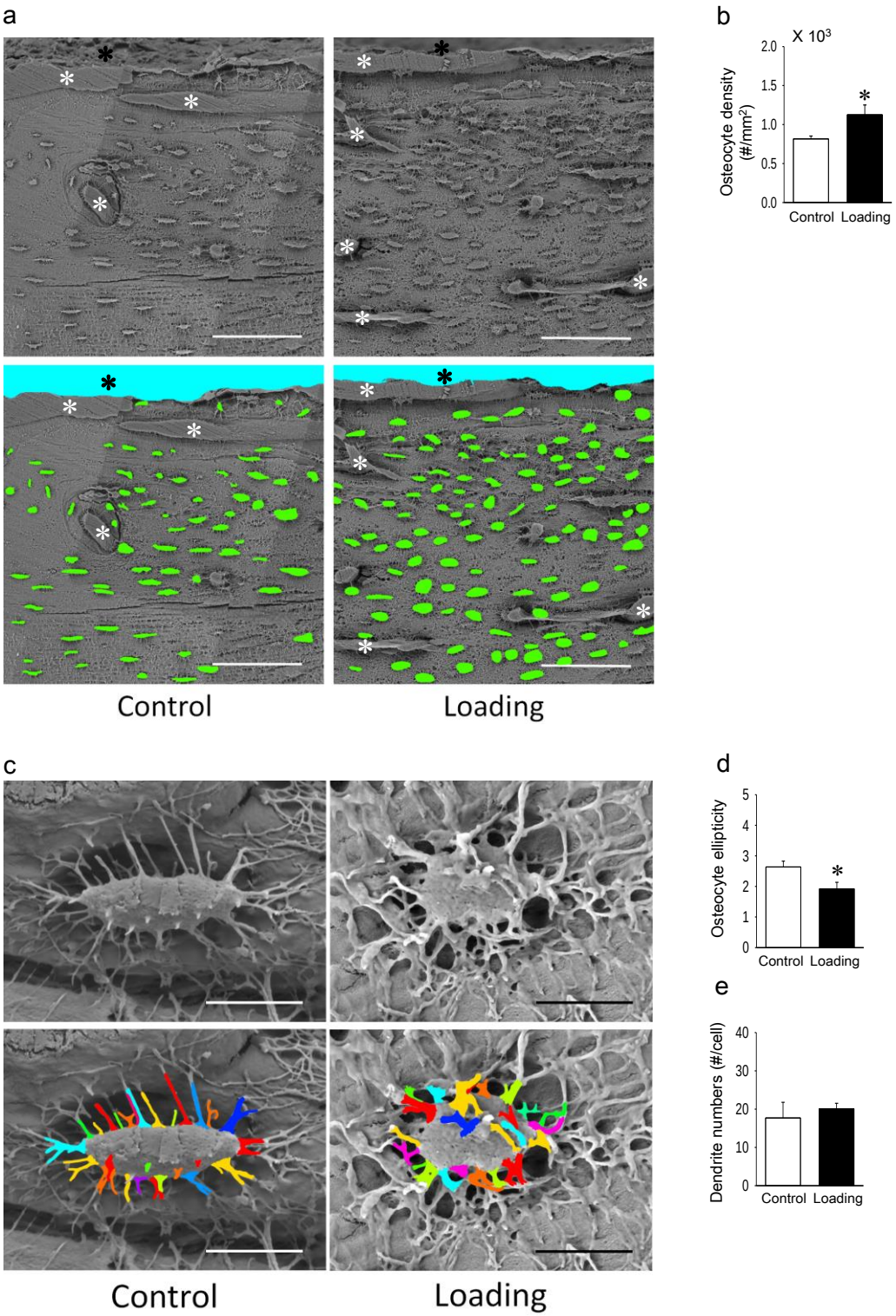
a
b
X 10³
Osteocyte density (#/mm²)
2.0
1.5
1.0
0.5
0.0
Control
Loading
Control
Loading
c
d
Osteocyte ellipticity
5
4
3
2
1
0
Control
Loading
e
Dendrite numbers (#/cell)
40
30
20
10
0
Control
Loading
Control
Loading

Fig. 8.

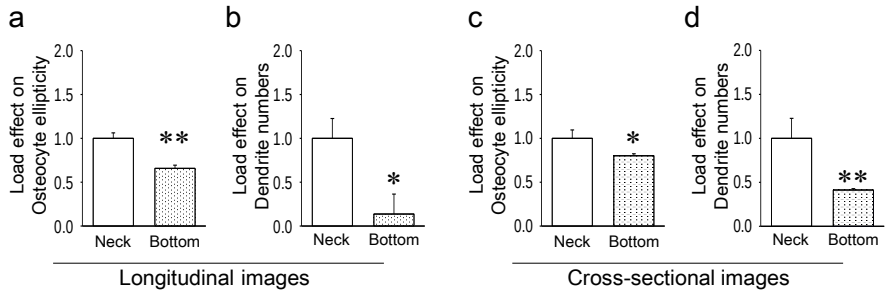
a
b
c
d
Load effect on Osteocyte ellipticity
Load effect on Dendrite numbers
2.0
1.5
1.0
0.5
0.0
**
*
Neck
Bottom
Longitudinal images
Cross-sectional images